Meteorol. Z. (Contrib. Atm. Sci.)
Published online May 2025

Open Access
Early Access Article Atmospheric Dynamics

Simulation of wind speed and wind turbine yield time series by a meso-micro downscaling approach

Heinz-Theo Mengelkamp*, Joachim Geyer, Markus Kilian, Martin Schneider

anemos Gesellschaft für Umweltmeteorologie mbH, Böhmsholzer Weg 3, 21391 Reppenstedt, Germany, www.anemos.de
* Corresponding author: mengelkamp@anemos.de

With 16 figures and 4 tables

Abstract: An efficient method to simulate time series of wind speed and wind turbine electricity generation on a microscale grid resolution is described. Speed-up factors are simulated by the microscale model *Meteodyn* for 12 wind direction sectors and 10 stability classes. The speed-up factors on the microscale grid are combined with wind speed time series simulated with the mesoscale model WRF (Weather Research & Forecasting Model) resulting in long-term wind speed time series on the microscale grid. Thermal effects are considered by translating the near-surface Monin-Obukhov-Length L which is a WRF output parameter into the stability classes defined by the CFD model *Meteodyn*.

Wind simulations are compared to LiDAR (Light Detection and Ranging) measurements at two sites during a summer and winter period showing an under- and overestimation, respectively. The vertical wind shear and the temporal variability are reasonably well simulated. The bias differs for the summer and winter period and depends on the meso-cell option selected for the microscale model forcing. The effect of this "representativeness error" is shown by comparing the vertical wind profile simulated with different mesoscale grid cell forcings.

The particular winter and summer case used here as an example show a different behavior. In summer wind speed is underestimated which results in an electricity production close to the one recorded by a nearby wind farm. The winter case for a different site shows an overestimation of the wind speed which would lead to unrealistic production data. Therefore, we correct for this bias by scaling the modelled wind speed at hub height to match on-site measurements by a LiDAR device. This correction will make the simulated electricity production comparable to the actual production which is deduced from an analysis of SCADA (Supervisory Control and Data Acquisition) data. No correction was necessary for the summer period. A site-specific correction factor will be essential for a realistic estimate of the wind turbine electricity production with an uncertainty as low as required for financial investments. On-site measurements and an adequate site-specific scaling of the simulated wind conditions will form the basis for reasonable site assessments.

Keywords: meso-microscale modelling; downscaling; wind potential; wind turbine electricity production

1 Introduction

With the increasing share of wind power in the electricity supply wind turbines have continuously become larger with respect to hub height and rated power and they will be placed more and more at complex sites. Investing into a wind farm requires knowledge of the electrical power output which corresponds to the revenue and similarly on the uncertainty of its estimation which corresponds to the risk of an investment. Increasing investment costs call for an uncertainty reduction of the long-term Annual Energy Production (AEP) estimation. If temporally varying power production restrictions were imposed on wind turbines for the protection of animals and/or for the avoidance of shadow and noise interferences a time series analysis is required for the loss calculation. A time dependent view of the electricity production is also essential for dealing on the stock exchange with demand dependent prices. These considerations call for accurate models and methods to simulate time series of the wind conditions and power production well above the surface layer and over complex terrain.

Traditional tools like the linear microscale model WAsP (Troen & Petersen 1989; Troen 1996) assume a logarithmic vertical wind profile for the AEP calculation based on a wind speed frequency distribution. These models simulate the long-term mean wind conditions and turbine power generation and are applicable primarily over flat terrain. In order to overcome the limitations of linear models and to simulate the atmospheric flow conditions even over complex sites and well above the surface layer atmospheric mesoscale models were introduced for wind potential estimations (Mahrer et al. 1985; Mengelkamp et al. 1997, Mengelkamp

DOI: 10.1127/metz/20242
Gebrüder Borntraeger Science Publishers, Stuttgart, www.borntraeger-cramer.com

1999; Brower et al. 2004). In order to increase the spatial resolution mesoscale-microscale coupling approaches have been developed (Badger et al. 2014; Haupt et al. 2019a, b; Durán et al. 2019, 2020). The mesoscale model commonly is a typical numerical weather prediction (NWP) model and the microscale model is of Computational Fluid Dynamic (CFD) type. Full-physics NWP models capture the dynamic and thermodynamic atmospheric time dependent processes but are limited in horizontal resolution down to approximately 1 kilometer. The more detailed wind characteristics in the immediate surrounding of a wind farm are simulated with a CFD model typically with a spatial resolution in the order of a few tens of meters. However, CFD models commonly assume neutral atmospheric conditions as they do not include thermodynamic processes. Attempts were made to consider the atmospheric stability in CFD simulations for the wind industry (Meissner et al. 2009; Durán et al. 2019; Hristov et al. 2014; Albrecht et al. 2014, Buhr et al. 2021, Chang et al. 2018). Hristov et al. (2014) compared the AEP calculation with production data from an existing wind farm. Using WAsP and a neutral CFD model they found an error of 16 % and 14 %, respectively. Considering stability and the diurnal cycle in the CFD simulation the AEP estimation error was reduced to 3 %. They conclude that a CFD model with stability included lowers the AEP calculation error. Considering the atmospheric stability reduces the uncertainty of the simulation of mean conditions and is indispensable for a time series simulation.

Nesting a fine-grid microscale model into a coarse-grid atmospheric mesoscale model is a common downscaling methodology. The essential atmospheric variables of the mesoscale model are used as boundary conditions for the fine-scale model at consecutive time steps (Olsen 2018). This approach is appropriate for high resolution short-term weather forecasts but not feasible for the wind industry due to its very high computational effort when used for long-term time series simulations. The alternative to this direct nesting is the modular nesting (Haupt et al. 2019b) or offline coupling. In the case of offline coupling the mesoscale information is taken from a transient mesoscale model and used to drive a stand-alone microscale model (Haupt et al. 2019b). The overall model chain then comprises a) a reanalysis data set providing the time series forcing for the mesoscale model, b) the mesoscale model supplying the statistics for the microscale model and c) the microscale model (Fig. 1).

For site assessment studies in the wind industry the mesoscale model forced by reanalysis data $u(t)_{macro}$ commonly is run in a transient mode $u(t)_{meso}$. The mesoscale time series

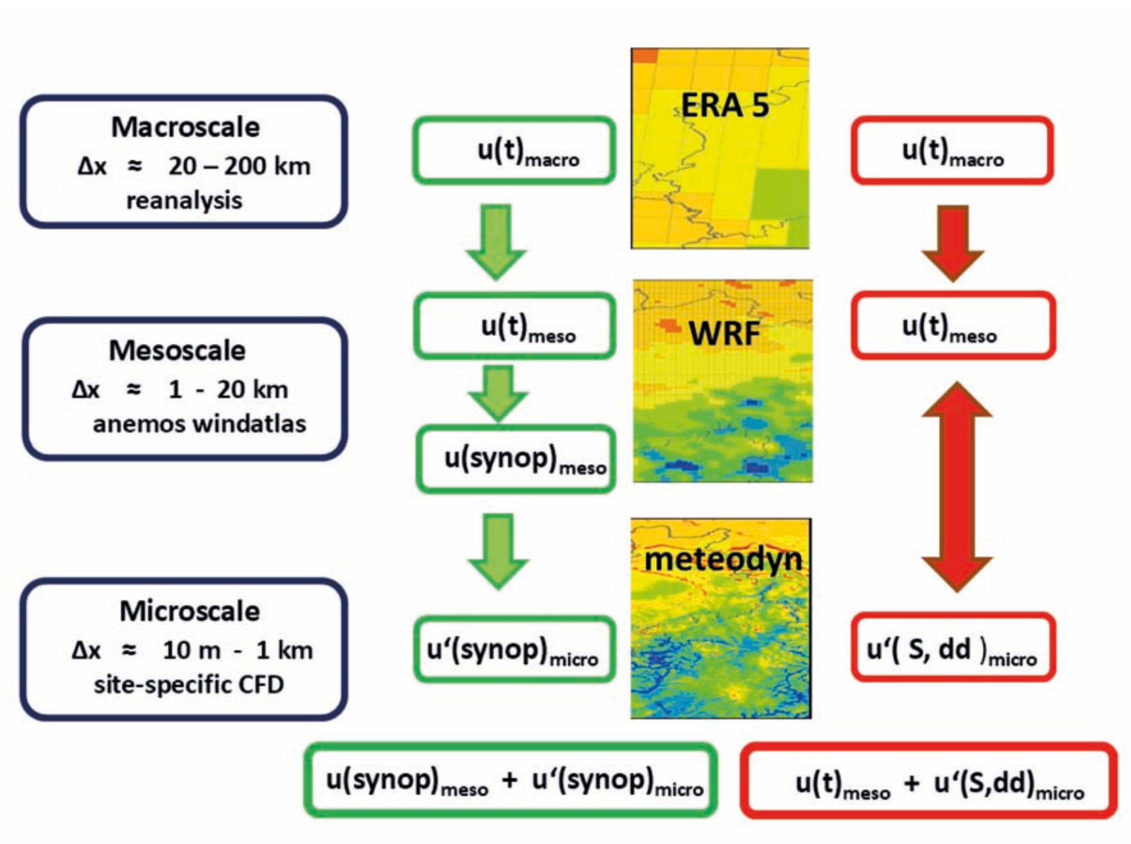

Fig. 1. Model chain from ERA5 reanalysis data to the WRF wind atlas simulation and finally to the *Meteodyn* CFD site specific simulations. Common statistical method framed green, time series simulation approach framed red.

$u(t)_{meso}$ is then classified into a statistic of weather types or synoptic situations $u(synop)_{meso}$ which represent the characteristics of the wind climate. The $u(synop)_{meso}$ classes are often defined by wind direction sector and stability. Steady-state simulations with the microscale model are performed for each of the synoptic classes $u(synop)_{meso}$ resulting in speed-up factors on the microscale grid for each of the synoptic classes $u'(synop)_{micro}$. Durán et al. (2019) applied the model chain CFSR (reanalysis data) – WRF (mesoscale model) – WindSim (CFD model, WINDSIM 2023) to investigate different strategies of the mesoscale-microscale coupling for different stability classes. A one-year WRF simulation was driven by CFSR reanalysis data. This one-year time series data set was sorted into 12 direction sectors and 4 stability classes. Steady state simulations with the CFD model WindSim were then performed for the 48 cases of WRF output. Hristov et al. (2014) run the WRF mesoscale model forced by GFS analyses for a period of 14 years and prepared a mesoscale climatology for stability conditions occurring within each of 36 directional sectors. A CFD model is then run for this climatology classification.

In order to reduce the computational effort even more Frank et al. (2001) and Badger et al. (2014) derived representative weather situations from the NCEP/NCAR reanalysis data (Kalnay et al. 1996) and performed mesoscale simulations for equidistant direction sectors and prescribed wind speed classes. The resulting frequency distribution from the mesoscale simulations is then used as input to the linear microscale model WAsP (Troen 1996; Troen & Petersen 1989).

Both approaches result in the long-term mean wind potential (framed green in Fig. 1). This has been and still is adequate for wind farm planning and financing purposes given a fixed feed-in tariff. However, a thorough revenue estimation considering time dependent losses and spot market prices requires a time series simulation of the power production rather than a long-term average. Buhr et al. (2021) simulate a one-year time series with a coupled meso-microscale approach similar to the one described in this paper. Their method is based on pre-calculated, independent mesoscale and microscale simulations with the wind climate being reduced to 36 wind direction sectors and 3 stability classes.

This paper aims at presenting a coupled meso-microscale modeling approach for wind speed time series simulations which still reasonably limits the computational effort and to finally estimate realistic numbers for the electricity production of wind turbines. We simulate the long-term time series with a mesoscale model driven by reanalysis data. The result is a wind atlas as described by Schneider et al. (2022). Independent of these transient mesoscale simulations, steady-state CFD simulations with the software *Meteodyn* are run in a statistical mode for 12 wind direction sectors and 10 stability classes using analytical boundary conditions. The resulting speed-up factors on the microscale grid are assumed independent of wind speed which is a reasonable assumption as they only depend on orography and hence on wind direction and on stability. The transient mesoscale wind at each time step is imposed onto these microscale speed-up factors for the respective stability class resulting in wind speed time series at microscale grid nodes. This method is framed red in Fig. 1.

Details of the mesoscale and microscale models and their set-up as well as the coupling approach are given in section 2 and the observational data are described in section 3. The comparison of the simulated with the observed data is shown in section 4 for two sites in moderately complex terrain. Section 5 comprises a summary and an outlook.

2 Numerical models and the coupling approach

2.1 The mesoscale model

The mesoscale model WRF (Weather Research & Forecasting Model, Skamarock et al. 2008) has been widely used in the context of wind energy over the last decade (Deppe et al. 2013; Giannakopoulou & Nhili 2014; Carvalho et al. 2014; Gopalan et al. 2014; Siuta et al. 2017; Weiter et al. 2019; Hahmann et al. 2020; Dörenkämper et al. 2020; Schneider et al. 2022). In this study WRF version 3.7.1 (the current version when we started the wind atlas simulation was not changed for consistency reasons) is used to downscale ERA5 reanalysis data (C3S 2017; Hersbach et al. 2020) with a horizontal resolution of approx. 30×30 km^2 to two domains with 9×9 km^2 for the outer domain and 3×3 km^2 for the inner nested domain to the region of Germany (Fig. 2). The vertical model structure is divided into 50 levels with 14 of them in the lowest 300 m. The upper boundary is at roughly 10 km height. The time period from 1997 until present is simulated

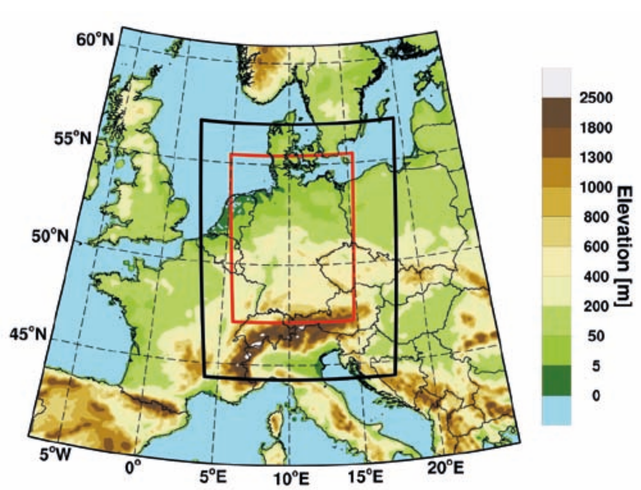

Fig. 2. WRF model domain over Germany. Multiple nesting with domain 1 (9×9 km^2, black) and domain 2 (3×3 km^2, red).

and model output is stored every 10 minutes. Instead of multiple re-initializations as suggested by Qian et al. (2003) a long-term continuous simulation is performed to avoid long spin-up times and potential discontinuities. The ERA5 data are nudged into the WRF model every hour which ensures stable continuous runs (Lo et al. 2008).

Vegetation and roughness information is taken from the CORINE data (Keil et al. 2010) of the European Environment Agency and is interpolated from its 100 m resolution. Soil temperature & soil moisture at 4 soil levels and snow cover are taken from the ERA5 data set (C3S 2017). Orography data are taken from the SRTM (Shuttle Radar Topography Mission, USGS EROS Data Center, Farr et al. 2007) and interpolated from its 90 m resolution onto the model grid. From the various WRF physics parameterization schemes we considered the Yonsei University (YSU) planetary boundary layer scheme, the Monin-Obukhov surface layer description, the Noah land surface model including Mosaic 4, the RRTM scheme for the longwave radiation, and the Dudhia parameterization for the short-wave radiation. No cumulus parameterization is applied (Skamarock et al. 2008).

Extensive sensitivity studies (Hu et al. 2010; Jiménez & Dudhia 2012; Olsen et al. 2017; Rai et al. 2019; Hahmann et al. 2020) reflect the uncertainty of model simulations with respect to parameter settings and model set-up rather than the difference to the "real world", namely observations. But the latter is of relevance for the wind industry. Therefore, an optimization approach ("remodeling" in the following) is applied to the WRF wind speed time series up to 300 m height. The remodeling process basically uses sub-grid information which is not part of the original WRF simulation to improve the wind speed model output. This includes the height of grid cell and the slope of the surface, the latitude, and the surface roughness. A detailed description of the remodeling approach is given in Weiter et al. (2019) and Schneider et al. (2022). Wind data from 28 observation sites in a height range of 80 to 140 m are used to develop an empirical relation between simulated and observed wind speed data depending on the height difference between the model grid average and the observation site. An empirical constant for the height correction was derived from high resolution computational fluid dynamic simulations. Differences due to surface roughness variations were accounted for by a linear regression analysis separately for 8 wind direction sectors. From the empirical relations at the 28 sites global scaling factors are derived which are applied to wind speed simulations for each of 8 wind direction sectors separately.

The results of the remodeling process were verified with data from 48 onshore met masts (including the 28 masts used for the derivation of the empirical correction factors) and with 66 masts by an independent external verification study cited in Schneider et al. (2022). While the raw uncorrected data show a mean positive bias of 0.7 m/s the remodeled data show a slight overcorrection and a mean negative bias of −0.4 m/s. In addition, the annual cycle was corrected by reducing the positive bias in winter and the negative bias in summer.

Schneider et al. (2022) show that the comparison of uncorrected WRF wind data with observations at more than 100 measurement sites results in an overestimation of wind speed of up to 20 % at most of the stations despite the fact that wind measurements for the wind industry are taken preferably at exposed and undisturbed sites. Jiménez & Dudhia (2012) speculate that the reason for the overestimation is the unresolved topographic features in a uniform mesoscale grid cell which neglect an additional drag imposed on the wind by small scale variable orography and vegetation. Overestimated wind conditions already by the forcing reanalysis data or non-optimal parameterizations in the mesoscale model may also add to this effect. The typical mesoscale bias in wind speed is corrected for by the remodeling process to a substantial part.

2.2 The microscale model *Meteodyn*

The commercial CFD model *Meteodyn* (Meteodyn 2024) is used for the microscale simulations. *Meteodyn* solves the Reynolds averaged Navier-Stokes equations of mass and momentum conservation for incompressible steady flow (RANS model). Turbulent fluxes are parameterized by using a one-equation turbulent kinetic energy (TKE) closure scheme. The TKE transport equation includes a dissipation term which depends on a turbulent length scale L. The impact of stratification onto the flow is parameterized by a K-L turbulence modeling and boundary conditions according to the Monin-Obukhov theory. The Monin-Obukhov similarity theory (MOST) may only be applied within the limit of a critical Richardson number. To account for strong stability cases outside this limit a four-layer scheme is introduced (Albrecht et al. 2014, Meteodyn 2022) which comprises (1) a dynamic layer up to two times the roughness element height which is dominated by mechanical effects at ground level, (2) the MOST layer with a critical Richardson number lower than 0.01 (Grachev et al. 2013) and a modification in the mixing length formulation to account for a limiting buoyancy length scale, (3) a transitional layer above the MOST layer with turbulent fluxes decreasing with height, and (4) the free atmosphere where the turbulent fluxes depend on the large-scale meso-scale turbulence. The effects of the thermal stability in CFD computations are considered by means of 10 thermal stability classes from very unstable (class 0) to very stable (class 9) (Meteodyn 2022).

Meteodyn is run in a stand-alone mode forced by an analytical wind profile consistent with the Monin-Obukhov-theory and 10 prescribed stability classes for each of 12 wind direction sectors into a steady-state solution. The result comprises 12 × 10 sets of speed-up ratios at each of the microscale grid nodes. The model domain covers an area of approximately 50 × 50 km^2 with a horizontal resolution of 20 m around the points of interest (e.g. the location of a met mast or the wind turbine site). An adaptive mesh expands towards the outer boundaries. The refinement and expansion are controlled by prescribed aspect ratios to avoid convergence instabilities. The numerical mesh is aligned with the flow direction at the inflow boundary. The vertical resolution is 4 m for the lowest 10 levels and then expanding with a coefficient of 1.2 up to 2.7 km height.

Orography is taken from a geo-database of Rhineland-Palatinate (DGM25 2024) with 25 m horizontal resolution and roughness data are taken from the CORINE land cover data set (CLCS-2018) and interpolated onto the respective model grid. A forest parameterization is activated in each grid cell if the roughness length multiplied by a prescribed forest factor is larger than 1.5 of the lowest vertical grid-cell. For the activated forest module, a sink term for momentum and a source term for turbulence are added to the respective equations (Meteodyn 2022). Wind farm wake effects are considered for in *Meteodyn* by a modified PARK model which is based on the equation for cluster efficiency (Katic et al. 1986) and calculates the wind speed reduction behind a wind turbine and the overlapping of wake influenced areas of several turbines. Power curves for the different turbine types were provided by the manufacturer and used as input to *Meteodyn* for power output estimations. The power curves are corrected for air density at each turbine site according to IEC 61400-12-1:2022 (IEC 61400 2022).

Table 1. Relation between *Meteodyn* stability classes and the Monin-Obukhov-Length *L*.

***Meteodyn* stability class**	**condition**	**L range [m]**
0	very unstable	$L > -1000$
1	unstable	$-5000 < L < -1000$
2	neutral	$\vert L \vert > 5000$
3	near neutral	$2600 < L < 5000$
4	slightly stable	$1700 < L < 2600$
5	stable	$950 < L < 1700$
6	stable	$550 < L < 950$
7	very stable	$200 < L < 550$
8	very stable	$70 < L < 200$
9	very stable	$0 < L < 70$

2.3 Coupling methodology

The idea of downscaling is the transfer of information on representative atmospheric conditions from the global scale (reanalysis data) to the mesoscale and down to the microscale (Fig. 1). While the reanalysis data and mesoscale models provide the information of typically all relevant physics on the global and regional scale the microscale model is supposed to add the small-scale orographic speed-up effects. Here, the mesoscale and microscale models are run independently. The mesoscale time series are taken from the wind atlas for Germany (Schneider et al. 2022). Running a microscale model in a transient mode over decades, however, is very computer resource consuming and expensive. We therefore run the microscale model for a synthetic frequency distribution given by 10 stability classes for each of 12 wind direction sectors. A synthetic wind profile is prescribed. Wind speed is specified internally and fixed as it is assumed that the speed-up factors are independent of wind speed. The resulting 120 tables of the speed-up factor at the microscale grid nodes provide the adaptation factors to the mesoscale time series of wind speed at each 10-minute time step according to wind direction and stability. The speed-up factor effective for the wind direction of the mesoscale time series is estimated by an inverse distance weighting of the speed-up factors of the two nearest direction sectors of the microscale tables. The stability classes are defined by the Monin-Obukhov-Length *L* at 10 m height above the surface which is an output parameter of WRF simulations and related to *Meteodyn* stability classes according to Table 1 (Meteodyn 2022).

A reasonable WRF simulation of the Monin-Obukhov-Length *L* and an adequate classification to the *Meteodyn* stability classes are critical for the coupling approach. Measurements of the sensible heat flux and the momentum flux to calculate *L* are rare and not available at our sites. But in order to get at least an idea of the reliability of the WRF simulated *L* we have compared these data with observations even though at a different site with different topographic characteristics. *L* was calculated from measurements of the sensible heat flux and the momentum flux at the Lindenberg observation tower of the German Weather Service (Beyrich personel communication). The area was also part of the WRF wind atlas simulations. Fig. 3 shows the majority of 30-min averages of *L* as observed and simulated in the period 2017–

Table 2. Observational data.

site	**device**	**hub height [m]**	**time period**	**comment**
A	1 x LiDAR		01.03.2022–31.07.2022	
	5 x ENERCON-E70 E4 5 x ENERCON-E70 E4 1 x ENERCON E82	113.5 85.0 85.0	01.01.2016–31.08.2022	monthly electricity production and availability
B	1 x LiDAR		02.09.2016–06.03.2017	
	6 x VESTAS V80–2.0	100.0	01.01.2016–31.08.2017	SCADA data

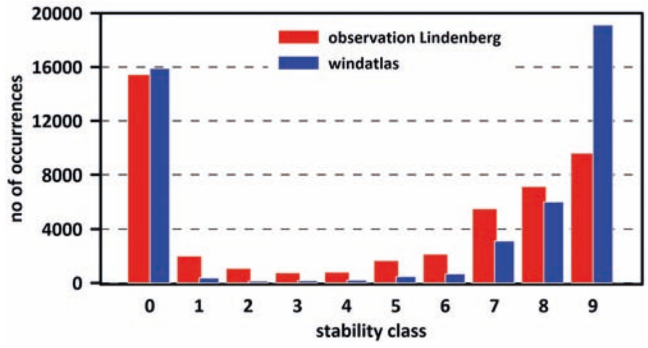

Fig. 3. The Monin-Obukhov-Length at 10 m height as measured at the Lindenberg tower (red) and as output of WRF (blue). 30-min averages for the period 2017–2019.

One could argue that microscale effects are double counted when applying remodeled mesoscale wind atlas data as forcing for a microscale model which in turn account for microscale effects. The wind atlas remodeling process basically is a correction of the systematic bias in wind speed for the mesoscale grid cell. From the comparison of the simulated wind speed with 26 distributed measurements global scaling factors were empirically derived and applied at each grid cell. This corresponds to steps 1 to 3 in chapter 4.1 of Schneider et al. (2022) resulting in empirically corrected mesoscale cell wind speed data. With the microscale simulation described here this remodeled mesoscale cell wind speed is corrected for site-specific surface characteristics in the surrounding of the LiDAR measurement location. This information is not used in the remodeling process because the LiDAR data were not among the 26 test measurements.

2019 for the very unstable (class 0) and stable (class 7, 8, 9) situations. Summing up the stable cases the coincidence of occurrences seems to be reasonable and no correction for L was applied although having in mind that a grid cell averaged parameter is compared to a point measurement.

In order to calculate the time series $u(t)_{meso} + u'(S,dd)_{micro}$ at the point of interest on the microscale grid the mesoscale time series $u(t)_{meso}$ is taken from one single grid cell (single point downscaling, preferably the mesoscale grid cell which includes the wind farm or the measurement device for a validation) or from several mesoscale grid cells (multi-point downscaling, preferably if the wind farm area covers several mesoscale grid cells). In case of a multi-point downscaling the time series at the points of interest are calculated by an inverse distance averaging of the mesoscale time series and the microscale speed-up factor at the site of interest. A similar coupling approach is followed by Buhr et al. (2021) who chose a different microscale statistic with 36 direction sectors but only 3 stability classes. They also found an overestimation of the wind speed by model simulations and corrected for this by linear interpolation with data from one met mast before comparing to a nearby second mast. Buhr et al. (2021) use mesoscale data from the NEWA project which generally overestimates wind speed (Schneider et al. 2022). Although claiming that their paper is intended for the wind energy industry Buhr et al. (2021) do not undertake the final step to wind turbine power production estimations.

The speed-up factors depend on height and are taken from the 3-d microscale tables according to the respective measurement height or hub height. In case the heights of the CFD simulations differ from the heights of interest a *Meteodyn* internal interpolation procedure calculated the suitable speed-up factor.

The advantage of this one-way coupling strategy with standalone simulations is that both, the mesoscale model and the CFD code, are run independently and no special coupling interface is required for the data transfer between them.

3 Observational data

To simulate time series of both, wind speed and wind turbine power output, two sites were selected at which wind speed measurements by a LiDAR device and SCADA data (Supervisory Control and Data Acquisition) of wind turbines were available at the same time. Exact site locations are not disclosed for confidentiality reasons but maps with the wind farm layout and LiDAR location as well as the analysis are presented with explicit permission of the data owner (WIWI 2022).

Both sites are located in the low mountain range of the Hunsrück in the western part of the federal state of Rhineland-Palatinate of Germany roughly 20 km apart. The terrain may be characterized as moderately complex with a height range of 120 to 750 m a.m.s.l. The land use is a mixture of forests and farmland.

At site A the LiDAR device was installed in a clearing within a dense forest (Fig. 4). Wind turbines in cell 1 and 3 of the mesoscale grid are located inside a forest while the turbines in cell 4 are surrounded by farmland stretching south-west to north-east but also close to a larger forest north and south.

At site B (Fig. 5) the turbines were placed inside a small forested area. The surrounding area is characterized by a continuous change of farmland and forests. The LiDAR device was located at the center south side of the wind farm in cell 2.

Wind speed and direction are measured by a Doppler Wind LiDAR windcube v2 (GWU 2023) at heights 40, 58, 83, 98, 112, 118, 138, 158, 165, 178, 198 and 218 m above ground level at site A which is 443 m a.m.s.l. Measuring heights for site B at 487 m a.m.s.l. were 42, 60, 80, 89, 100, 120, 140, 150, 159, 166, 180, and 200 m, respectively. Installation and verification reports are available which makes the data being considered reliable. The Carrier-to-Noise-Ratio (CNR) threshold is internally set to −23 not

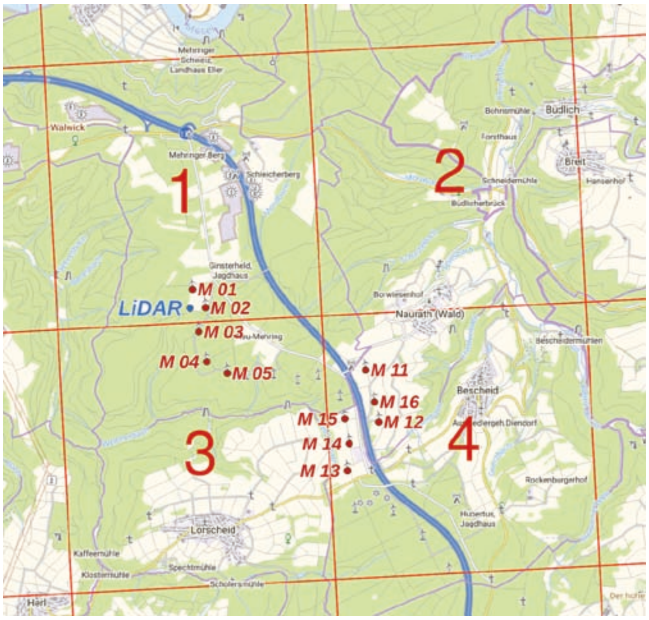

Fig. 4. Layout of the wind farm (red dots) at site A, the LiDAR position (blue dot) and the WRF grid cells (Source: Bundesamt für Kartographie und Geodäsie 2024 (https://basemap.de/, https://www.bkg.bund.de), Lizenz: CC BY 4.0 (https://creativecommons.org/licenses/by/4.0/))

considering measured data below this value. The availability varied from 99,95 % at 40 m height to 98,71 % at 200 m height for site A and 98,90 % at 40 m height to 90,75 % at 200 m for site B, respectively.

A few small periods of missing data between 10 min and 3 hours duration occurred particularly at larger heights above 140 m. These gaps were filled by interpolation but are irrelevant for this study as turbine hub heights do not exceed 113.5 m.

SCADA systems in wind turbines comprise a large number of operational parameters including the electricity production at 10 min intervals. A SCADA data analysis allows the correction of the electricity production for periods of non-optimal turbine operation. Quite often turbines are shut down or run in a reduced mode due to regulatory restrictions for noise reduction and animal protection (bats and birds) or exceedance of the electrical grid. These losses are not considered in the simulations. Therefore, turbine power data are filtered precisely in order to obtain a data set which can be compared to the simulated turbine power output. Corrections with regard of status codes or by comparison with nearby turbines on a 10 min basis resulted in power data for an optimal operation mode. The SCADA data analysis met the requirements of the Technical Guideline TR 10 (FGW 2021) which describes in detail how to correct for faulty yield data. Wake effects are included and not corrected for as they are also accounted for in the CFD simulations which makes the data directly comparable. SCADA data were available for 6

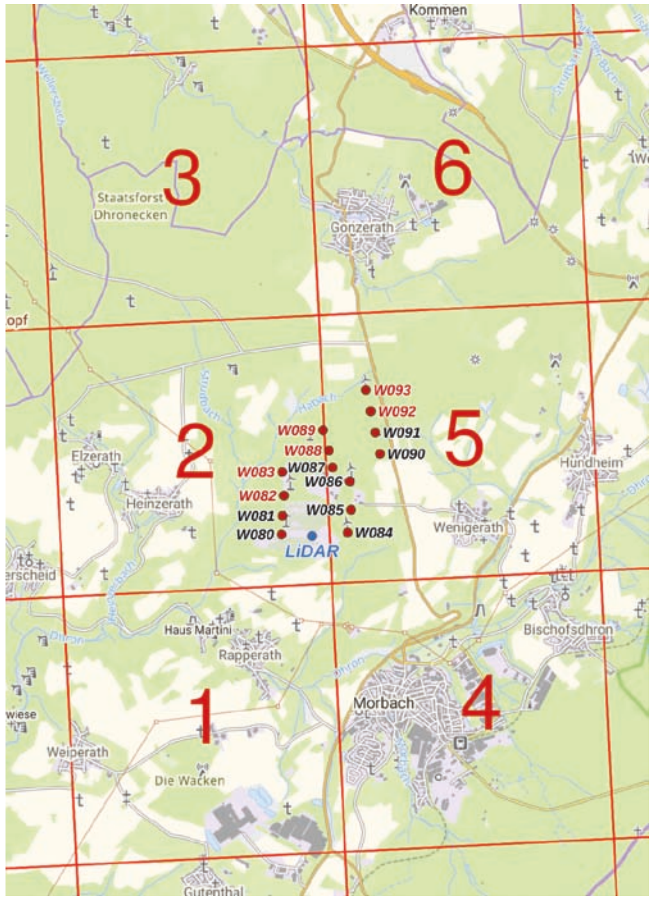

Fig. 5. Layout of the wind farm (red dots) at site B, the LiDAR position (blue dot) and the WRF grid cells. The identification of the six analyzed wind turbines is typed red) (Source: Bundesamt für Kartographie und Geodäsie 2024 (https://basemap.de/, https://www.bkg.bund.de), Lizenz: CC BY 4.0 (https://creativecommons.org/licenses/by/4.0/)). Scada data were available from turbines W082, W083, W088, W089, W092, W093.

(W082, W083, W088, W089, W092, W093 in Fig. 5) out of 14 turbines of wind farm at site B.

For site A only monthly production data and turbine availability were provided for 11 out of 12 wind turbines. In this case the missing data were replaced by a potential production based on average wind conditions during the respective month to generate a time series with 100 percent availability. Any uncertainty due to non-optimal operation modes is not accounted for and considered acceptable.

4 Results

4.1 Wind speed

For the period of the LiDAR measurements observed and simulated wind speed data are compared in terms of mean vertical profiles, the diurnal cycle, and time series. The vertical wind speed profiles are used to investigate the “representativeness error" which is explained in Jiménez & Dudhia (2012) and Jiménez et al. (2010). They refer to the fact that uncertainties are involved when comparing numerical simulation results with in-situ observations. The spatial discretization inherent for a model smooths the orography and vegetation distribution and the simulated variable represents a model grid volume with homogeneous properties rather than an observation at a specific point. This may lead to the fact that the model grid cell encompassing the observation site may not necessarily be the most suitable one to represent the observation. Nearby grid cells may be more appropriate. We will address this issue by simulating the mean vertical wind speed profile with input from each of the nearest mesoscale cells and with a multi-cell forcing (average of nearest cells). Fig. 6 shows that the profile for the summer period at site A simulated with mesoscale data from grid cell 2 is closest to the observed profile particularly in the height range of 80 to 140 m relevant for the wind turbine hub heights. Forcing with grid cell 1 in which the LiDAR is located results in the largest underestimation. The "representativeness error" at 100 m height between the measurements and the cell 1 wind speed profile is roughly 0.3 m/s or about 7 percent. The profiles reflect the forest influence below 80 m height. Wind farm wake effects shape the profiles to the left between 80 and 170 m height. Above this height the wake and forest effects decline. Overall, the simulated profiles are close to the observed one. Because the wind farm is spread over three mesoscale grid cells the multi cell option is applied for the following additional analyses and for the wind turbine yield estimation.

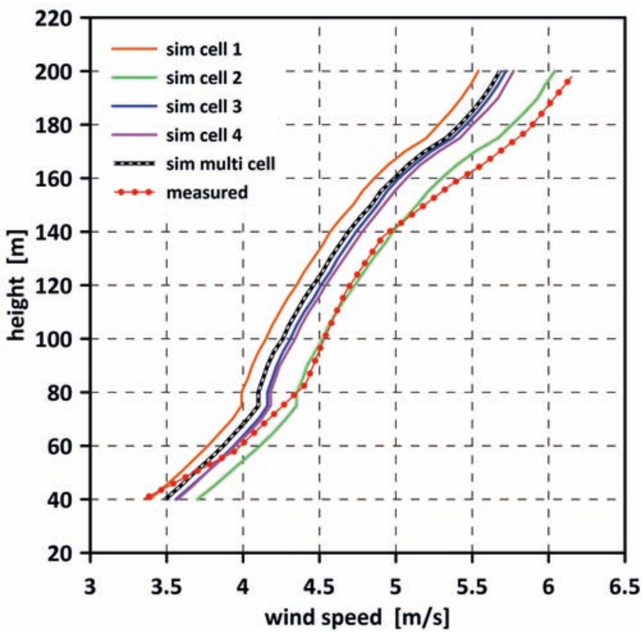

Fig. 6. Mean vertical wind speed profiles at site A during the LiDAR period as measured (red dots) and simulated with CFD forcing from each of 4 grid cells and their average (multi cell).

Statistical measures in Table 3 show an underestimation of the mean wind conditions. The standard deviation and the maxima are higher for the simulated time series. The correlation increases with height and with increasing averaging period as expected.

For months September to February at site B (Fig. 7) the measured wind speed is overestimated over the entire height range and amounts to roughly 10 percent at 100 m height for all forcing options except the one with cell 6 which shows a large difference while all other cell forcings are close. Although sites A and B are close (roughly 20 km) with similar surface characteristics a remarkable difference is seen when comparing simulated and observed wind speed profiles. The underestimation in summer and the overestimation in winter may be caused by a bias in the annual cycle still showing an overshooting of wind speed during winter times in the WRF simulations despite a correction of the annual cycle (Schneider et al. 2022).

This behavior is reflected in the wind speed statistics (Table 4) which cannot directly be compared to Table 3 as they were measured during a different season. The standard

Table 3. Statistical measures for measured and simulated wind speed time series at site A. Mean wind speed u_m, standard deviation of wind speed σ_u, maximum u_{max} and minimum u_{min} 10-min average and the correlation coefficient R for 10-min. hourly, 3-hourly, and daily averages.

Site A	measured 10-min average			simulated 10-min instantaneous		
	60 m	100 m	140 m	60 m	100 m	140 m
u_m	3.9	4.5	4.9	3.8	4.2	4.6
σ_u	1.69	2.08	2.43	2.14	2.37	2.60
u_{max}	14.2	17.1	19.7	19.2	20.4	21.5
u_{min}	0.3	0.2	0.3	0.2	0.4	0.5
$R_{10\text{-min}}$	0.70	0.76	0.78	x	x	x
R_{hourly}	0.73	0.79	0.82	x	x	x
$R_{3\text{-hourly}}$	0.78	0.84	0.86	x	x	x
R_{daily}	0.90	0.95	0.95	x	x	x

Table 4. Statistical measures for measured and simulated wind speed time series at site B. Mean wind speed u_m, standard deviation of wind speed σ_u, maximum u_{max} and minimum u_{min} 10-min average and the correlation coefficient R for 10-min. hourly, 3-hourly, and daily averages.

Site B	measured 10-min average			simulated 10-min instantaneous		
	60 m	100 m	140 m	60 m	100 m	140 m
u_m	4.0	4.9	5.6	4.9	5.6	6.3
σ_u	2.55	2.89	3.17	2.83	3.17	3.48
u_{max}	21.4	25.0	26.3	21.2	22.5	23.5
u_{min}	0.1	0.0	0.0	0.4	0.5	0.5
$R_{10\text{-min}}$	0.81	0.83	0.85	x	x	x
R_{hourly}	0.85	0.86	0.87	x	x	x
$R_{3\text{-hourly}}$	0.88	0.89	0.90	x	x	x
R_{daily}	0.94	0.95	0.95	x	x	x

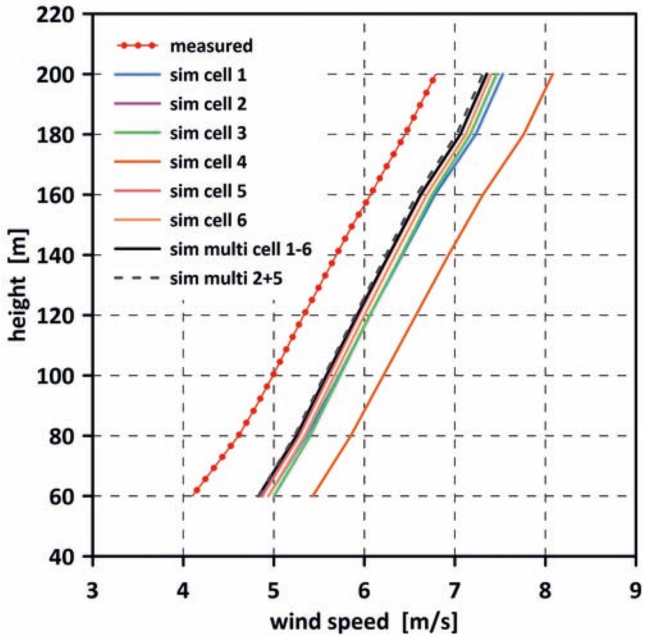

Fig. 7. Mean vertical wind speed profiles at site B during the LiDAR period September 2, 2016–March 6, 2017 as measured (red dots) and simulated with CFD forcing from each of 6 grid cells and their weighted average (6 cells and cells 2 + 5). Forcing is WRF time series at 300 m height.

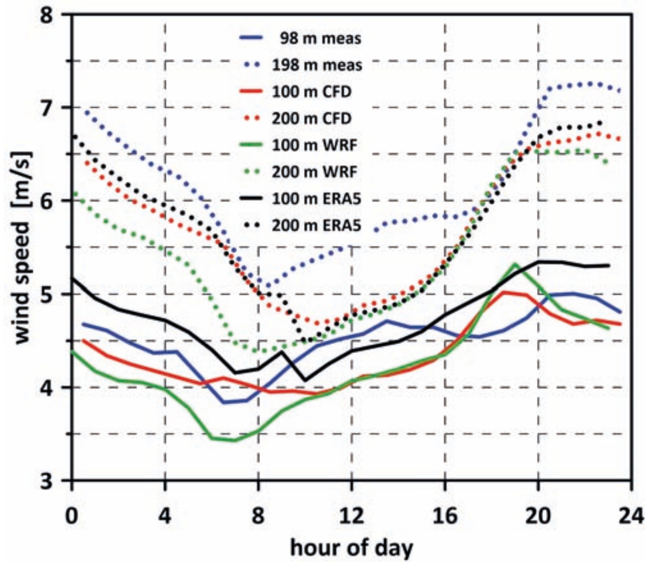

Fig. 8. Diurnal cycle of the wind speed at the LiDAR location at site A, measured (meas), simulated (sim) with WRF, simulated with *Meteodyn* (CFD), and the corresponding ERA5 data at 100 m and 200 m for the period March 1–July 31, 2022.

deviation and the maxima at site B are larger than those for site A. The correlation coefficients are higher for the winter period at site B. At both sites the vertical wind shear is close to observations.

The electrical power output of wind turbines is commonly overestimated even if the wind conditions were simulated accurately. The reason is likely a difference between the "official" and the on-site turbine power curve (see chapter 4.2). Calculating the turbine power output based on the already overestimated wind simulated for site B would make no sense. The mesoscale simulated wind speed for site B is therefore scaled by a factor of 0.89 (relation between measured and simulated mean wind speed at 100 m height). The scaled wind speed is applied for any further analysis. Scaling simulated wind conditions with on-site measurements is a common approach in commercial site assessment studies to reduce the uncertainty to a minimum and to provide realistic electricity production estimates to wind farm investors for their financial consideration. In order to make this possible a site assessment study typically is a combination of on-site measurements and model simulations.

The mean diurnal cycle of the wind speed during the LiDAR measuring period is shown for the ERA5 data and the WRF grid cell which encompasses the LiDAR measurement for the summer period at site A (Fig. 8) and the winter

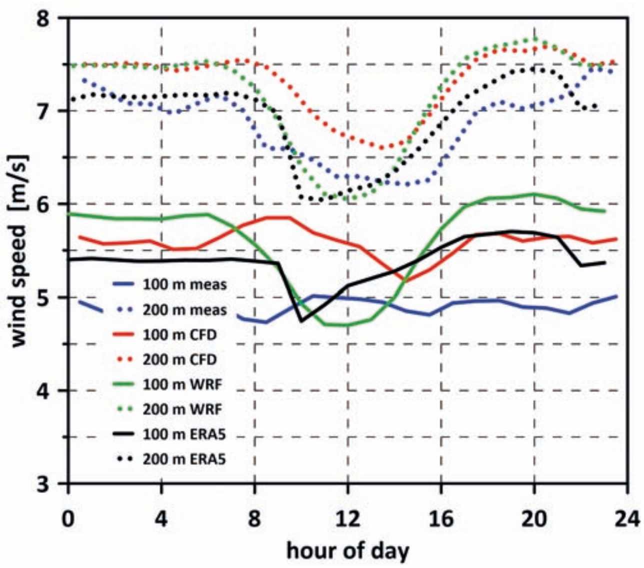

Fig. 9. Diurnal cycle of the wind speed at the LiDAR location at site B, measured (meas), simulated (sim) with WRF, simulated with *Meteodyn* (CFD), and the corresponding ERA5 data at 100 m and 200 m for the period September 2, 2016–March 6, 2017.

period at site B (Fig. 9) for 100 m and 200 m together with the measurements and microscale simulations for heights 100 m and 200 m which is the relevant height range for today's wind turbines. At site A (Fig. 8) the characteristics of the diurnal cycle of the ERA5 and WRF data are well reflected by the CFD simulations with kind of a minimum before (100 m) and around (200 m) hour 8 and a gradual increase during daytime.

At 100 m and to a larger extent at 200 m height all simulations underestimate the measurements particularly between hour 8 and 16. A maximum in the WRF and CFD simulations at 100 m height around hour 19 is not reflected in the ERA5 data nor by the measurements. The latter actually show a slight minimum between hour 16 and 20. The unrealistic step in the ERA5 data between 0900 and 1000 hours is a known artifact (ECMWF 2017).

During the winter months at site B the diurnal cycle of the wind speed (Fig. 9) shows only small variations in the measurements at 100 m height while a minimum is indicated in the simulations yet at different times of the day and with different amplitudes. At 200 m height all simulations and the measurements are much more in agreement with a pronounced minimum during daytime. With respect to the difference of the absolute values it should be noted that the WRF wind speed forcing the CFD simulations is scaled by a factor 0.89 for site B.

The agreement of the temporal variation of simulated and measured wind speed also becomes obvious from the time series of the daily values over a period of 6 and 7 months at sites A (Fig. 10) and site B (Fig. 11), respectively. There is a tendency of overestimating the maxima and underestimating the minima at site A. At site B the scaling prevents a larger overestimation.

4.2 Electrical power production

The relation between wind speed and electrical power production is given by the respective wind turbine's power curve. The latter is provided by the manufacturer and measured under idealized conditions (IEC 61400 2022). Usually, wind farm site characteristics differ from the idealistic ones (complex orography and roughness conditions with high turbulence versus flat and uniform terrain with low turbulence) in a way that the real power production of a turbine in operation is lower than the one simulated with the manufacturer's power curve. In addition, regulatory specifications may lead to a slow-down or even a cut-off of a turbine during specific time periods. An overestimation of the real power output by the theoretical yield is common. The official power curves (Fig. 12) as provided by the manufacturers were used to estimate the turbine energy yield. The power curves were corrected for air density according to IEC 61400-12-1:2022 (IEC 61400 2022) assuming a constant value deduced from height corrected weather station data (site A: weather station Lingen at 24 m a.m.s.l. with 9.4 °C mean temperature, site B: weather station Cologne-Wahn at 92 m a.m.s.l. with 9.6 °C mean temperature).

The monthly recorded electricity production of the turbines at site A (M 01 to M 04: ENERCON E70 E4 2 MW with 113,5 m hub height, M 11 to M 15: ENERCON E70 E4 2 MW with 85 m hub height, M 16: ENERCON E82 2.3 MW with 85 m hub height) during the LiDAR period in Fig. 13 shows a maximum in April 2022 combined with the largest spread among the turbines. The recorded values are overestimated by the simulated ones by up to more than 40 percent (turbines M 11, M 13 and M 16 in April in Fig. 14). There is not a consistent picture with regard to the respective turbine type and hub height. The largest temporal variation is seen for turbines M 12 and M 13. The yield of some turbines is underestimated to a small extent in June and July. Weather conditions (wind speed and wind direction) and surface characteristics at the particular sites (height a.m.s.l. and roughness) may influence the over- and underestimation. The average overestimation of the 10 turbines during the LiDAR period amounts to 18 percent. The monthly availability of the turbines ranges from 85 percent to 93 percent which is low compared to an expected availability of more than 97 percent for soundly operating turbines. The uncertainty related to the non-availability correction is not quantifiable as the time periods of non-availability and consequently the wind conditions are not known. Therefore, the average conditions during the particular month are assumed for the periods of non-availability even if the turbines may have been down during conditions of high or very low wind speeds. Despite these deficiencies we have analyzed this site A case as both, wind speed measurements and production data from operat-

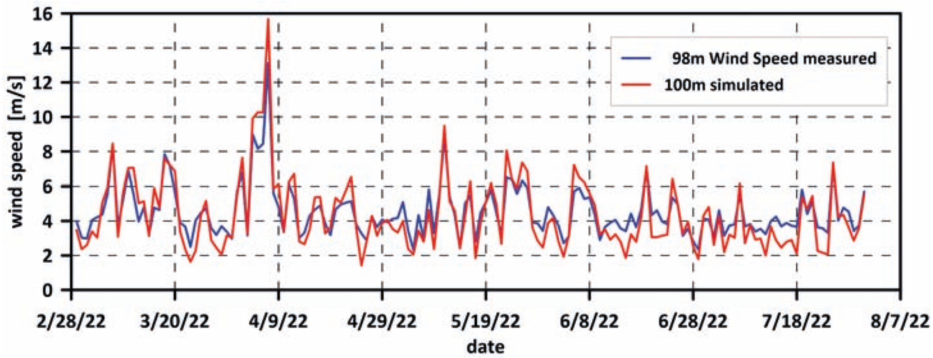

Fig. 10. Time series of daily wind speed averages at 98 m (measured) and 100 m (simulated) height at site A for the period March 1–July 31, 2022.

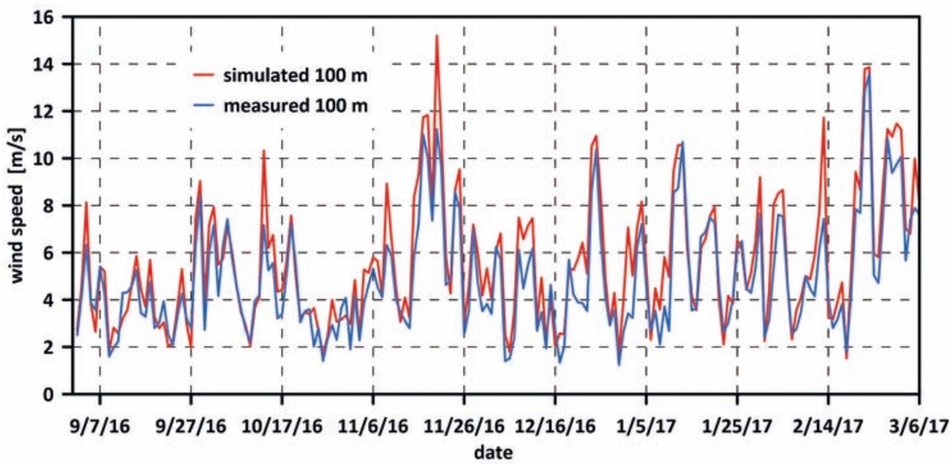

Fig. 11. Time series of daily averages of measured and simulated (scaled by 0.89) wind speed at 100 m height at site B for the period September 01, 2016–March 06, 2017.

ing turbines were available for the same time period. This hardly is the case as wind speed measurements are usually performed during the pre-operational phase.

In order to minimize or exclude some of the uncertainties for the comparison a virtual turbine (ENERCON E70 E4 2 MW with 83 m hub height) was placed at the LiDAR location and its yield was simulated for the LiDAR period. Applying the same power curve and hub height the turbine yield was also calculated based on the actual LiDAR data. Averaged measured and simulated wind speed resulted to 4.4 m/s and 4.1 m/s (Fig. 6) while the power production was 584 MWh and 550 MWh, respectively. This difference is mainly due to the fact that the simulation was forced with the multi-cell option. Forcing with meso-cell 1 in which the LiDAR was placed shows a larger difference while only a small difference in wind speed at 83 m height (Fig. 6) is seen when forcing with meso-cell 2. This shows the relevance of the "representativeness error" mentioned by Jiménez et al. (2010). The differences in electrical power output would have changed accordingly depending on turbine type and hub height.

Monthly production data and the corresponding availability of the ten turbines at site A were provided for more than 6 years (January 2016 to August 2022). Averaging over all turbines and all months results in an overestimation of 33 percent with a range from 15 (turbine M01) to 49 (turbine M 11) percent among the turbines. The maximum overestimation for a single turbine in a particular month is 126 percent (turbine M 02 in October 2018) followed by 105 percent for turbine M 13 in October 2019. The minimum monthly relation between simulated and real production for a single turbine is in a range from 77 percent (23 percent underestimation for turbine M 02) to 117 percent (17 percent overestimation for turbine M 16). The time series of the simulated and recorded monthly electricity production of the whole wind farm (Fig. 15) show a general overestimation during winter months corresponding with the fact of a biased annual cycle which obviously is not corrected for to the extend necessary.

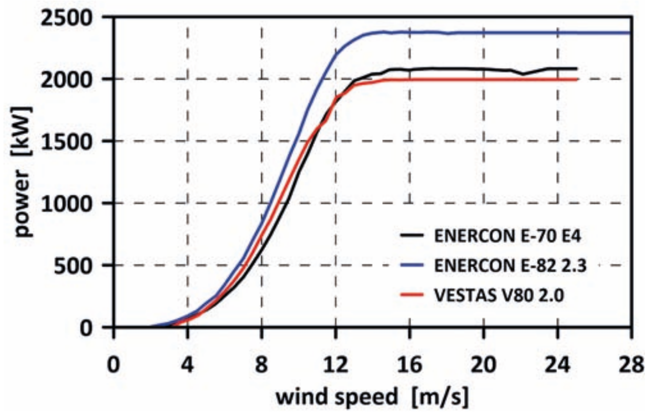

Fig. 12. Power curves for wind turbines at site A and site B.

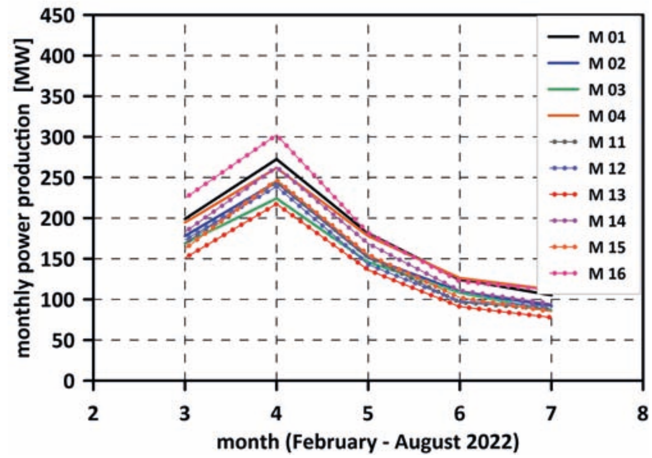

Fig. 13. Monthly real power production of turbines at site A during the LiDAR period for turbines M01–M04 and M11–M16.

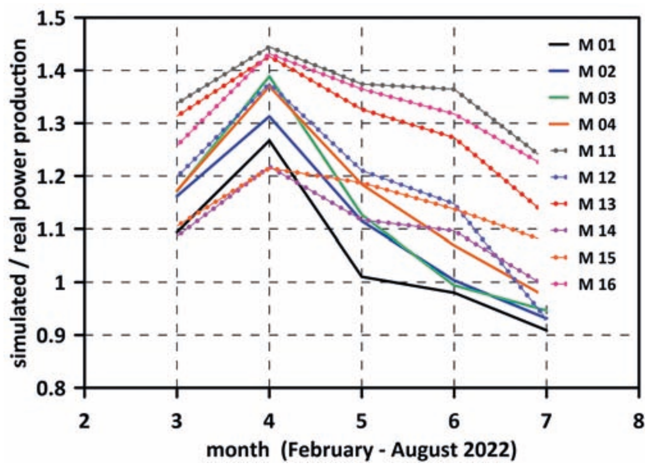

Fig. 14. Relation of simulated monthly power production to real production of turbines M01–M04 and M11–M16 at site A during the LiDAR period.

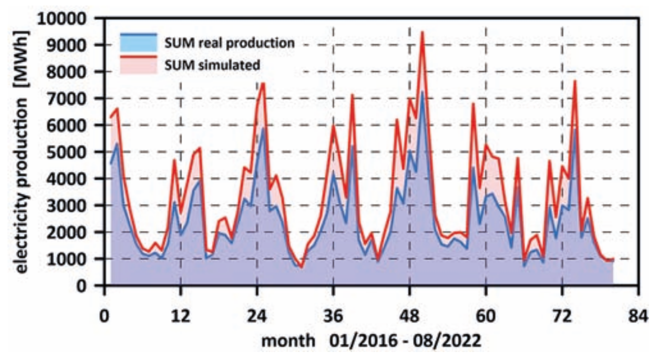

Fig. 15. Sum of monthly electricity production of turbines 1–4 and 11–16 at site A for the period January 2016–August 2022.

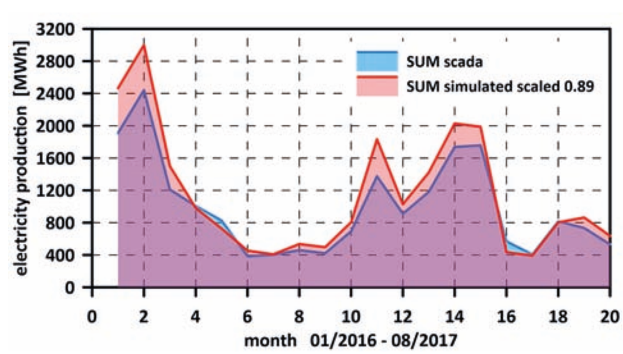

Fig. 16. Sum of monthly electricity production of all turbines at site B, simulated (wind speed scaled by 0.89) and SCADA data for the period January 2016–August 2017.

An overestimation of the recorded power production by a wind simulation in combination with the official power curve is a common feature because no turbine operates in an optimal mode. Whether the turbines at site A occasionally run in a reduced mode is not known. The only information is the monthly production and the corresponding monthly availability. The latter ranges from 84 to 94 percent over all turbines and for the whole time period of 80 months. Similar as for the production data during the Lidar period this analysis is based on the monthly power production corrected for non-availability to 100 percent assuming average monthly conditions during the non-operating time periods. There is a huge range of uncertainties on the side of the power production reported by the turbine operator but also on the modelling part. With the multi-cell forcing the wind speed was underestimated at site A. The parameterization of forests in the mesoscale and the microscale simulation may not reflect the real conditions and may contribute to the unexpected large overestimation.

With the relatively large overestimation of the wind speed at site B (Fig. 7) and the assumption that an overestimation of the electrical power output is common when calculated by the official power curve even with correct wind conditions an unrealistic overassessment of the power output at site B is obvious. Indeed, the power output of the 6 wind turbines during the time period January 2016 to August 2017 is overestimated by 55 percent with the non-scaled wind speed. The uncertainty of the real production can be considered low as 10-min SCADA data were available. With the scaled wind speed the overestimation of the power output is reduced to 15 percent averaged over all turbines and months. An overestimation during winter months is visible (Fig. 16). The time varying bias in the mesoscale data (Schneider et al. 2022) is obviously not sufficiently corrected for.

5 Conclusion and outlook

This paper presents a downscaling approach from the mesoscale to the microscale which allows the simulation of long-term time series on the microscale grid with reasonable computational effort. Instead of representing the long-term wind climate by a statistic of weather conditions on the mesoscale, speed-up factors are simulated by the microscale model independently for a prescribed statistic given by wind direction sectors and stability classes. The speed-up factors on the microscale grid are combined with the wind speed time series on the mesoscale grid resulting in long-term wind speed time series on the microscale grid.

Compared to measurements of wind speed with a LiDAR device the simulated data showed an underestimation at site A and an overestimation at site B. A major reason might be a non-sufficient correction of the annual cycle. Maxima are overestimated at both sites. The mean diurnal cycles during the measurement periods as well as the long-term time series are reasonably well captured demonstrating that the information on the atmospheric stability is appropriately transferred from the mesoscale model to the microscale simulations. The mean vertical wind shear is simulated similarly to the observed one.

From the uncertainties of wind speed and electrical power output simulations discussed in this paper we conclude that on-site measurements for the adaptation of wind simulations are indispensable if the site assessment study formed the basis for wind farm planning and financing purposes. The modification of simulation results based on the comparison of simulated and recorded electricity production data seems to be a major challenge as the information on the operation mode of existing wind turbines and the application of a site-specific power curve are usually not provided.

The many components of the overall uncertainty on the wind simulation part are e.g. the representation of surface characteristics in models, the parameterization of boundary layer physics, the transfer of stability information from the mesoscale model to the microscale model and the choice of mesoscale data to force the microscale model ("representativeness error"). The uncertainty of the turbine power output estimation basically consists of the lack of knowledge of the site-specific behavior of the turbine which commonly differs from the official power curve.

The verification of power output simulations with real data from operating wind turbines is a major challenge. Detailed information on the turbine operation status and regulatory restrictions as well as a careful analysis of the SCADA data are required in addition to the power curve issue.

The scaling factors (1 at site A, 0.89 at site B) depend on the location and time period of the measurements. There is no general rule of how to correct wind simulations but a site-specific adaptation will be required for realistic wind turbine power estimations. The path to realistically simulate wind conditions and turbine power output and minimizing the uncertainty without on-site measurements seems to be a long one. A large number of long-term wind measurements up to about 200 m height at different sites would be required to investigate reasons for differences between measurements and simulations and to overcome those deviations by general correction rules considering a wide range of site-specific surface characteristics. The remodeling approach described by Schneider et al. (2022) may be a first but promising step.

Acknowledgements: The study was supported in the framework of the SUnDAY (Simulation Uncertainty of the Detailed Assessment of wind turbine energy Yields) project funded by the Federal Ministry for Economic Affairs and Climate Action (BMWK). Our special thanks go to Dr. Jörn Parplies and Franziska Kreling of WIWI consult GmbH & Co. KG who provided the wind and SCADA data and gave permission for publication as done in this paper. We also thank Julian Ohl and Krischan Lingel for the LiDAR data analysis and Dr. Frank Beyrich of the German Weather Service who kindly provided the data of the Lindenberg met tower. Carsten Albrecht of AL-PRO GmbH & Co. KG helped to overcome many pitfalls in Meteodyn handling. Comments by two reviewers were much appreciated and helped to improve the paper.

References

Albrecht, C., Delaunay, D., Grötzner, A., Kohlert, M., & Pauschnere, L. (2014). Atmospheric stability: general classification and simulation in meteodyn *WT*. https://meteodyn.com/science-center/renewable-energy/125-atmospheric-stability-general-classification-and-simulation-in-meteodyn-wt.html

Badger, J., Frank, H., Hahmann, A. N., & Giebel, G. (2014). Wind-climate estimation based on mesoscale and microscale modeling: Statistical-dynamical downscaling for wind energy applications. *Journal of Applied Meteorology and Climatology*, *53*(8), 1901–1919. https://doi.org/10.1175/JAMC-D-13-0147.1

Brower, M., Zack, J. W., Bailey, B., Schwartz, M. N., & Elliott, D. L. (2004). *Mesoscale modeling as a tool for wind resource* *assessment and mapping*. Proceedings of the 14th conference on applied climatology

Buhr, R., Kassem, H., Steinfeld, G., Alletto, M., Witha, B., & Dörenkämper, M. (2021). A Multi-Point Meso-Micro Downscaling Method Including Atmospheric Stratification. *Energies*, *14*(4), 1191. https://doi.org/10.3390/en14041191

Carvalho, D., Rocha, A., Gómez-Gesteira, M., & Silva-Santos, C. (2014). WRF wind simulation and wind energy production estimates forced by different reanalyses: Comparison with observed data for Portugal. *Applied Energy*, *117*, 116–126. https://doi.org/10.1016/j.apenergy.2013.12.001

C3S–Copernicus Climate Change Service (C3S) (2017). ERA5: Fifth generation of ECMWF atmospheric reanalyses of the global climate. Copernicus Climate Change Service Climate Data Store (CDS). https://cds.climate.copernicus.eu/cdsapp#!/home

Chang, C.-Y., Schmidt, J., Dörenkämper, M., & Stoevesandt, B. (2018). A consistent steady state CFD simulation method for stratified atmospheric boundary layer flows. *Journal of Wind Engeneering and Industrial Aerodynamics, 172*, 55–67. https://doi.org/10.1016/j.jweia.2017.10.003

CLCS (2018). https://gdz.bkg.bund.de/index.php/default/corine-land-cover-5-ha-stand-2018-clc5-2018.html

Deppe, A. J., Gallus, W. A., Jr., & Takle, & E. S. (2013). A WRF ensemble for improved wind speed forecasts at turbine height. *Weather and Forecasting*, *28*(1), 212–228. https://doi.org/10.1175/WAF-D-11-00112.1

DGM25 (2024). https://lvermgeo.rlp.de/geodaten-geoshop/open-data

Dörenkämper, M., Olsen, B. T., Witha, B., Hahmann, A. N., Davis, N. N., Barcons, J., … Mann, J. (2020). The Making of the New European Wind Atlas – Part 2: Production and evaluation. *Geoscientific Model Development*, *13*(10), 5079–5102. https://doi.org/10.5194/gmd-13-5079-2020

Durán, P., Meissner, C., Rutledge, K., Fonseca, R., Martin-Torres, J., & Adaramola, M. S. (2019). Meso-microscale coupling for wind resource assessment using averaged atmospheric stability conditions. *Meteorologische Zeitschrift*, *28*(4), 273–291. https://doi.org/10.1127/metz/2019/0937

Durán, P., Meissner, C., & Casso, P. (2020). A new meso-microscale coupled modelling framework for wind resource assessment: A validation study. *Renewable Energy*, *160*, 538–554. https://doi.org/10.1016/j.renene.2020.06.074

ECMWF (2017). https://confluence.ecmwf.int/display/CKB/ERA5%3A+data+documentation#heading-Knownissues

FGW (2021). *Technical Guideline TR 10 – Determination of Site Quality after Commissioning, Revision 3, Federation of Wind and other Decentralized Energies*. FGW.

Farr, T. G., Rosen, P. A., Caro, E., Crippen, R., Duren, R., Hensley, S., … Alsdorf, D. (2007). The Shuttle Radar Topography Mission. *Reviews of Geophysics*, *45*(2), 2. https://doi.org/10.1029/2005RG000183

Frank, H. P., Rathmann, O., Mortensen, N. G., Landberg, L., & Petersen, E. L. (2001). The numerical wind atlas- The KAMM/WAsP method. In P. Helm & A. Zervos (Eds.), *Wind energy for the new millennium. Proceedings* (pp. 661–664). WIP – Renewable Energies.

Giannakopoulou, E.-M., & Nhili, R. (2014). WRF Model Methodology for Offshore Wind Energy Applications. *Advances in Meteorology*, *2014*, 319819. https://doi.org/10.1155/2014/319819

Gopalan, H., Gundling, C., Brown, K., Roget, B., Sitaraman, J., Mirocha, J. D., & Miller, W. O. (2014). A coupled mesoscale-microscale framework for wind resource estimation and farm aerodynamics. *Journal of Wind Engineering and Industrial Aerodynamics*, *132*, 13–26. https://doi.org/10.1016/j.jweia.2014.06.001

Grachev, A., Andreas, E., Fairall, C., Guest, P., & Persson, P. (2013). The critical Richardson number and limits of applicability of local similarity theory in the stable boundary layer. *Boundary-Layer Meteorology*, *147*(1), 51–82. https://doi.org/10.1007/s10546-012-9771-0

GWU (2023). GWU-Umwelttechnik GmbH. https://www.lidar.gwu-umwelttechnik.de/index.php/doppler-wind-lidar/windcube/windcube-onshore.html

Hahmann, A. N., Sîle, T., Witha, B., Davis, N. N., Dörenkämper, M., Ezber, Y., … Söderberg, S. (2020). The Making of the New European Wind Atlas, Part 1: Model Sensitivity. *Geoscientific Model Development*, *13*(10), 5053–5078. https://doi.org/10.5194/gmd-13-5053-2020

Haupt, S. E., Berg, L., Churchfield, M., Kosovíc, B., Mirocha, J., & Shaw, W. (2020). 2019a: Mesoscale to Microscale Coupling for Wind Energy Applications: Addressing the Challanges. *Journal of Physics: Conference Series*, *1452*(1), 012076. https://doi.org/10.1088/1742-6596/1452/1/012076

Haupt, S. E., Kosovíc, B., Shaw, W., Berg, L., Churchfield, L. K., Cline, M., … Sever, G. (2019b). On bridging a modeling scale gap: Mesoscale to microscale coupling for wind energy. *Bulletin of the American Meteorological Society*, *100*(12), 2533–2550. https://doi.org/10.1175/BAMS-D-18-0033.1

Hersbach, H., Bell, B., Berrisford, P., Hirahara, S., Horányi, A., Muñoz-Sabater, J., … Thépaut, J.-N. (2020). The ERA5 global reanalysis. *Quarterly Journal of the Royal Meteorological Society*, *146*(730), 1999–2049. https://doi.org/10.1002/qj.3803

Hristov, Y., Oxley, G., & Žagar, M. (2014). Improvement of AEP Predictions Using Diurnal CFD Modelling with Site-Specific Stability Weightings Provided from Mesoscale Simulation. *Journal of Physics: Conference Series*, *524*, 012116. https://doi.org/10.1088/1742-6596/524/1/012116

Hu, X.-M., Nielsen-Gammon, J. W., & Zhang, F. (2010). Evaluation of Three Planetary Boundary Layer Schemes in the WRF Model. *Journal of Applied Meteorology and Climatology*, *49*(9), 1831–1844. https://doi.org/10.1175/2010JAMC2432.1

IEC 61400 (2022). IEC 61400-12-1:2022, Wind energy generation systems – Part 12-1: Power performance measurements of electricity producing wind turbines, International Electrotechnical Commission. https://webstore.iec.ch/publication/68499

Jiménez, P. A., González-Rouco, J. F., García-Bustamente, E., Navarro, J., Montávez, J. P., Vilá-Guerau De Arellano, J., … Muñoz-Roldán, A. (2010). Surface wind regionalization over complex terrain: Evaluation and analysis of a high-resolution WRF numerical simulation. *Journal of Applied Meteorology and Climatology*, *49*(2), 268–287. https://doi.org/10.1175/2009JAMC2175.1

Jiménez, P. A., & Dudhia, J. (2012). Improving the representation of resolved and unresolved topographic effects on surface wind in the WRF model. *Journal of Applied Meteorology and Climatology*, *51*(2), 300–316. https://doi.org/10.1175/JAMC-D-11-084.1

Katic, L., Højstrup, J. & Jensen, N. O. (1986). A Simple Model for Cluster Efficiency, *European Wind Energy Association Conference and Exhibition*, Italy

Kalnay, E., Kanamitsu, M., Kistler, R., Collins, W., Deaven, D., Gandin, L., … Joseph, D. (1996). The NCEP/NCAR 40 year reanalysis project. *Bulletin of the American Meteorological Society*, *77*(3), 437–471. https://doi.org/10.1175/1520-0477(1996)077<0437:TNYRP>2.0.CO;2

Keil, M., Bock, M., Esch, T., Metz, A., Nieland, S. & Pfitzner, A. (2010). CORINE Land Cover Aktualisierung 2006 für Deutschland. Abschlussbericht zu den F+E Vorhaben UBA FKZ 3707 12 200 und FKZ 3708 12 200. Deutsches Zentrum für Luft- und Raumfahrt e.V., Deutsches Fernerkundungsdatenzentrum Oberpfaffenhofen, Januar 2010

Lo, J. C.-F., Yang, Z.-L., & Pielke, R. A., Sr. (2008). Assessment of three dynamical climate downscaling methods using the Weather Research and Forecasting (WRF) model. *Journal of Geophysical Research*, *113*(D9, D09112), 1–16. https://doi.org/10.1029/2007JD009216

Mahrer, Y., Segal, M., & Pielke, R. (1985). Mesoscale modelling of wind energy over non-homogeneous terrain. *Boundary-Layer Meteorology*, *31*(1), 13–23. https://doi.org/10.1007/BF00120031

Meissner, C., Gravdahl, A. R., & Steensen, B. (2009). Including thermal effects in CFD wind flow simulations. *Journal of Environmental Science International*, *18*(8), 833–839. https://doi.org/10.5322/JES.2009.18.8.833

Mengelkamp, H.-T., Kapitza, H., & Pflüger, U. (1997). Statistical-dynamical downscaling of wind climatologies. *Journal of Wind Engineering and Industrial Aerodynamics, 67–68*, 449–457. https://doi.org/10.1016/S0167-6105(97)00093-7

Mengelkamp, H.-T. (1999). Wind climate simulation over complex terrain and wind turbine energy output estimation. *Theoretical and Applied Climatology*, *63*(3-4), 129–139. https://doi.org/10.1007/s007040050098

Meteodyn (2022). Meteodyn Universe Microscale Advanced Notes, Meteodyn user manual

Meteodyn (2024). https://meteodyn.com/business-sectors/renewable-energy/meteodyn-universe/meteodyn-Universe/

Olsen, B. T., Hahmann, A. N., Sempreviva, A. M., Badger, J., & Jørgensen, H. E. (2017). An intercomparison of mesoscale models at simple sites for wind energy applications. *Wind Energy Science, 2*(1), 211–228. https://doi.org/10.5194/wes-2-211-2017

Olsen, B. T. (2018). Mesoscale to microscale coupling for determining site conditions in complex terrain, DTU Wind Energy. DOI:https://doi.org/10.11581/00000036

Qian, J.-H., Seth, A., & Zebiak, S. (2003). Reinitialized versus Continuous Simulations for Regional Climate Downscaling. *Monthly Weather Review*, *131*(11), 2857–2874. https://doi.org/10.1175/1520-0493(2003)131<2857:RVCSFR>2.0.CO;2

Rai, R. K., Berg, L. K., Kosović, B., Haupt, S. E., Mirocha, J. D., Ennis, B. L., & Draxl, C. (2019). Evaluation of the impact of horizontal grid spacing in terra incognita on coupled mesoscale-microscale simulations using the WRF framework. *Monthly Weather Review*, *147*(3), 1007–1027. https://doi.org/10.1175/MWR-D-18-0282.1

Schneider, M., Glücksmann, A., Grötzner, A., & Mengelkamp, H.-T. (2022). A wind atlas for Germany and the effect of remodeling. *Meteorologische Zeitschrift*, *31*(2), 117–130. https://doi.org/10.1127/metz/2022/1102

Siuta, D., West, G., & Stull, R. (2017). WRF hub-height wind forecast sensitivity to PBL scheme, grid length, and initial condition choice in complex terrain. *Weather and Forecasting*, *32*(2), 493–509. https://doi.org/10.1175/WAF-D-16-0120.1

Skamarock, W. C., Klemp, J. B., Dudhia, J., Gill, D. O., Barker, D. M., Duda, M. G.… Powers, J. G. (2008). A description of the advanced research WRF Version 3. NCAR Technical Note NCAR/TN-475+STR, 113 pp, June 2008

Troen, I. (1996). The WAsP code. In D. P. Lalas & C. F. Ratto (Eds.), *Modelling of atmospheric flow fields* (pp. 435–444). World Scientific. https://doi.org/10.1142/9789814447164_0018

Troen, I., & Petersen, E. L. (1989). *European Wind Atlas*. Denmark, Roskilde: RISØ National Laboratory for the Commission of the European Communities.

Weiter, A., Schneider, M., Peltret, D., & Mengelkamp, H.-T. (2019). Electricity production by wind turbines as a means for the verification of wind simulations. *Meteorologische Zeitschrift*, *28*(1), 69–77. https://doi.org/10.1127/metz/2019/0924

WINDSIM (2023). https://windsim.com/, homepage for the windsim CFD model

WIWI (2022). wiwi consult GmbH & Co. KG, personal communication, https://wiwiconsult.de/

Manuscript received: July 18, 2024
Revisions requested: November 16, 2024
Revised version received: January 7, 2025
Manuscript accepted: March 17, 2025